NONLINEAR ULTRASONIC NDT FOR EARLY DEFECT RECOGNITION AND IMAGING

Igor SOLODOV, Nils KROHN, and Gerd BUSSE
INSTITUTE OF POLYMER TECHNOLOGY, DEPARTMENT OF NONDESTRUCTIVE TESTING (IKT-ZFP), UNIVERSITY OF STUTTGART,
Pfaffenwaldring 32, 70569 Stuttgart, Germany

1. Introduction

A rapid growth of new high-tech materials used in safety critical applications imposes stringent requirements to manufacturing reliability, quality assurance of industrial products and health monitoring of existing components. This evokes development of a new generation of NDT methodologies with much greater sensitivity to incipient micro-defects and progressive damage. Conventional ultrasonic NDT equipment is normally a mono-frequency instrument which makes use of the amplitude and phase variations of the input signal due to its scattering by defects. One can bear with such inadequate amount of information as long as the wave-defect interaction is considered to be linear. The new approach which is believed to substantially extend frontier in NDT is concerned with application of nonlinear methods.

A traditional view on nonlinear ultrasonics is associated with classical idea of elastic wave distortion due to material nonlinearity: waveform deformation caused by a local velocity variation accumulates with propagation distance and provides progressive transition of a harmonic wave into sawtooth- or N-type waves. As a result, the spectrum acquires higher (ultra-) harmonics of the fundamental frequency which deliver information on the matter. In classical (free from defects) media, the material nonlinearity is quite low and normally only few harmonics are observable so that classical nonlinear NDT is basically “second harmonic NDT”.

The nonlinear approach to ultrasonic NDT (NNDT) developed over the last decade is concerned with nonlinear response of defects, which is related to extreme frequency changes of the input signal. These spectral changes are caused by anomalously high nonlinearity of micro- and macro-scale defects. The intact parts of the material outside the defect vibrate linearly, i.e. with no frequency variation in the output spectrum. Thus, in NNDT, a small cracked defect (transparent in a linear ultrasonic NDT) behaves as an ***active*** radiation source of new frequency components rather than a ***passive*** scatterer in conventional ultrasonic testing. This makes the NNDT a unique defect-selective instrument for localising and imaging of nonlinear flaws. The latter include a numerous class of contact defects, scaled from dislocations (nano-scale) to fatigue (micro-) cracks and macro-debonds in joints. Since the micro-contact (nonlinear) defects are only the forerunners of further major damage, the NNDT is thus capable of early recognition of material degradation and “predicting” the oncoming fracture.

In this paper, basic mechanisms responsible for frequency conversion by nonlinear defects are discussed and major features of the nonlinear spectra derived. Experimental methodologies of nonlinear scanning laser vibrometry (NSLV) and nonlinear air-coupled emission (NACE) are developed and used to study nonlinear elastic wave-defect interactions. Applications for defect-selective imaging and NNDT are demonstrated for a series of hi-tech materials and industrial components.

2. Higher harmonic generation by defects

Nonlinear response of cracked defects is provided by the higher-order Contact Acoustic Nonlinearity (CAN) [1] caused by mechanical constraints between the fragments of the defects that makes their vibrations extremely nonlinear and supports multiple ultra-harmonics as well as multi-wave interactions. The CAN generally manifests in a wide class of damaged materials and develops diversely for longitudinal and shear driving tractions which activate different mechanisms of nonlinearity.

2.1 "Clapping" mechanism

Consider a pre-stressed crack (static stress σ^0) driven by longitudinal acoustic traction $\sigma_\sim$ (Fig. 1) which is strong enough to provide clapping of the crack interface. The clapping nonlinearity comes from asymmetrical dynamics of the contact stiffness: the latter is higher in a compression phase (due to clapping) than that for tensile stress when the crack is assumed to be supported only by edge-stresses.

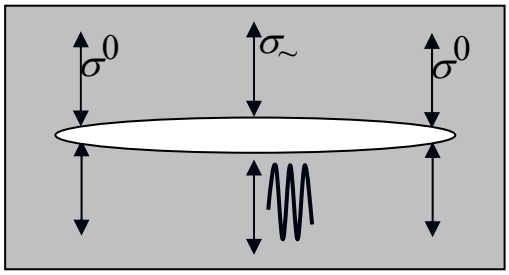

Fig. 1. Model of a clapping crack.

Such behaviour of a clapping interface can be approximated by a piece-wise stress (σ)-strain (ε) relation [2]:

$$\sigma = C[1 - H(\varepsilon)(\Delta C / C)]\varepsilon\,, \tag{1}$$

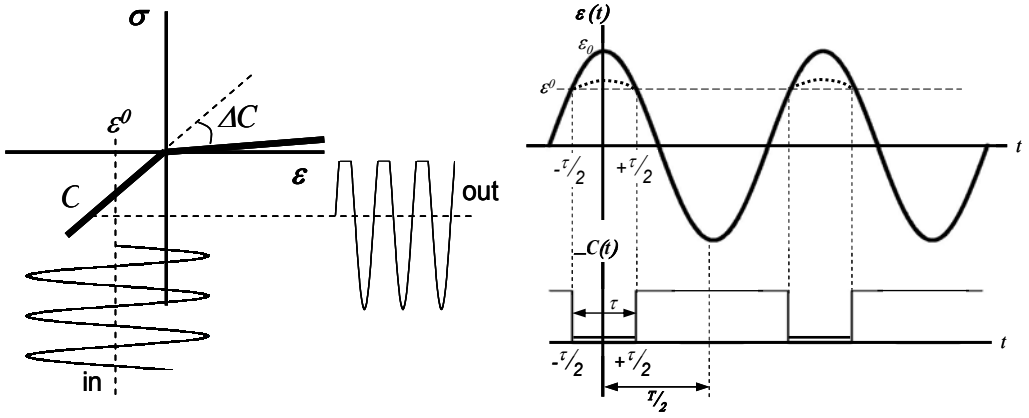

Fig. 2. Mechanical diode model (left); stiffness modulation and waveform distortion (right).

where $H(\varepsilon)$ is the Heaviside unit step function; $\Delta C = [C - (d\sigma / d\varepsilon)_{\varepsilon>0}]$, and C is the intact material (linear) stiffness.

The bi-modular pre-stressed contact driven by a harmonic acoustic strain $\varepsilon(t) = \varepsilon_0 \cos \nu t$ is similar to a "mechanical diode" and results in a pulse-type modulation of its stiffness $C(t)$ (Fig. 2). It also provides an unconventional nonlinear waveform distortion: a half-period rectified output (Fig. 2) instead of the saw-tooth like profile in classical materials. Since $C(t)$ is a pulse-type periodic function of the driving frequency ν (Fig. 2, right), the nonlinear part of the spectrum induced in the damaged area ($\sigma^{NL}(t) = \Delta C(t) \cdot \varepsilon(t)$) contains a number of its higher harmonics $n\nu$ (both odd and even orders) whose amplitudes are modulated by the *sinc*-envelope function [3]:

$$A_n = \Delta C \Delta \tau \varepsilon_0 \, [sinc((n+1)\Delta\tau) - 2cos(\pi\Delta\tau)sinc(n\Delta\tau) + sinc((n-1)\Delta\tau)]\,, \tag{2}$$

where $\Delta\tau = \tau / T$ ($\tau = (T/\pi) Arc\cos(\varepsilon^0 / \varepsilon_0)$ is the normalized modulation pulse length.

The spectrum of the nonlinear vibrations (2) is illustrated in Fig. 3, left and contains a number of both odd and even higher harmonics arising simultaneously as soon as $\varepsilon > \varepsilon^0$ (threshold of clapping). The *sinc*-modulation in (2) is amplitude dependent: as the wave amplitude ε_0 increases, τ grows from 0 to $T/2$. This affects the envelope of the harmonic amplitude oscillations and their dynamic characteristics (Fig. 3, right) due to the spectrum "compression" effect.

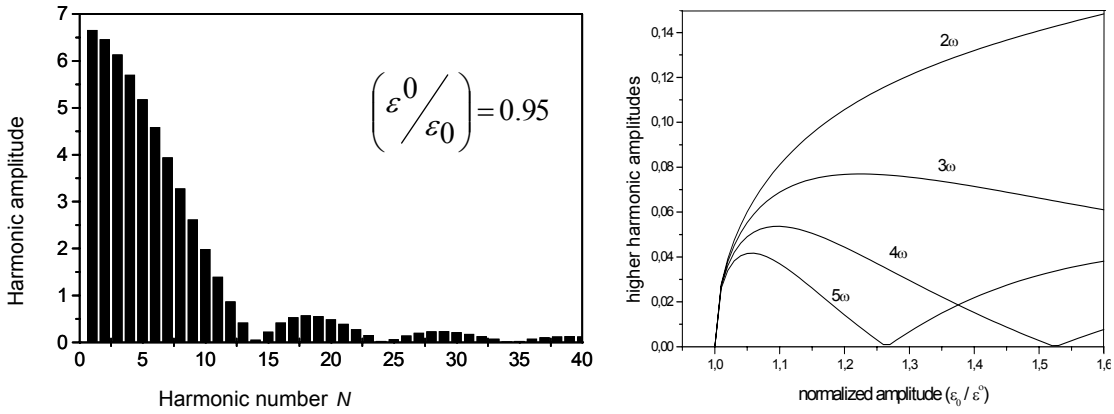

Fig. 3. CAN higher harmonic spectrum (left) and dynamic characteristics (right).

2.2 Nonlinear friction mechanisms

For a shear wave drive, the surfaces of the contact interface are mechanically coupled by the friction force caused by the interaction between asperities (Fig. 4). If the driving amplitude is small enough, the interface shear motion is constrained by the interaction between neighbouring asperities that prevents the contact surfaces from sliding (micro-slip mode). The mechanical diode model for the micro-slip motion is shown in Fig. 5, left and demonstrates a step-wise increase in tangential stiffness as the neighbouring asperities interact. This interaction is independent of the direction of shear motion and causes stiffness variation twice for the input signal period (Fig. 5, right). Such a constraint introduces a symmetrical nonlinearity and provides only odd harmonic generation. Like for the clapping mechanism, their amplitudes are *sinc*-modulated due to pulse-type stiffness variation [4] (Fig. 6):

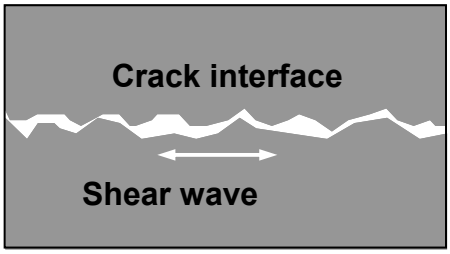

Fig. 4. Crack interface in shear traction.

$$A_{2N+1} = 2\Delta C \varepsilon_0 \left(\frac{\tau}{T}\right)\left\{\text{sinc}\left(\frac{2N\tau}{T}\right) + \text{sinc}\frac{2(N+1)\tau}{T}\right\} \tag{3}$$

and exhibit similar non-power dynamics.

When the amplitude of tangential traction is greater than the contact static friction force the micro-slip motion changes for sliding. A harmonic shear wave drive (strain ε) is accompanied by a cyclic transition between static and kinematic friction (stick-and-slide mode) so that the contact stress-strain relation follows a hysteric loop (Fig. 7) [3]. The contact tangential stiffness changes symmetrically (independent of the direction of motion) between the static C_s

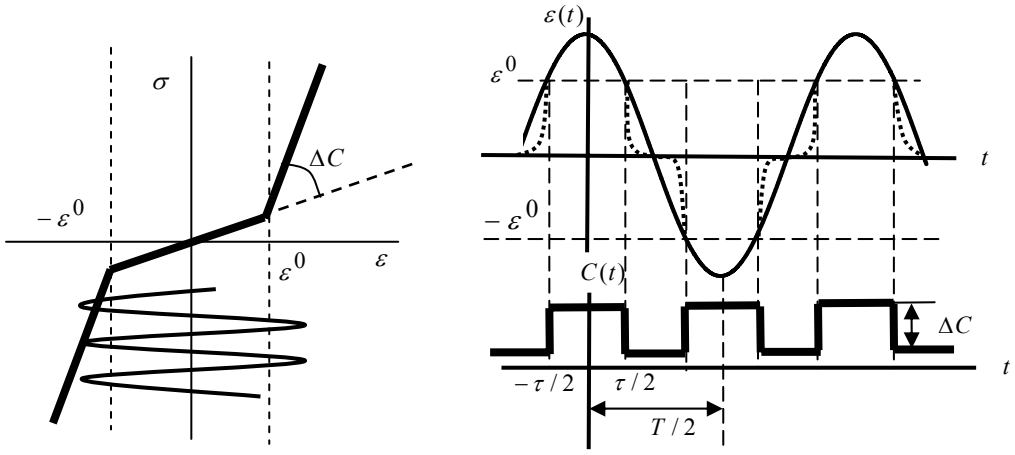

Fig. 5. Mechanical diode model (left), stiffness modulation and waveform distortion in micro-slip mode (right).

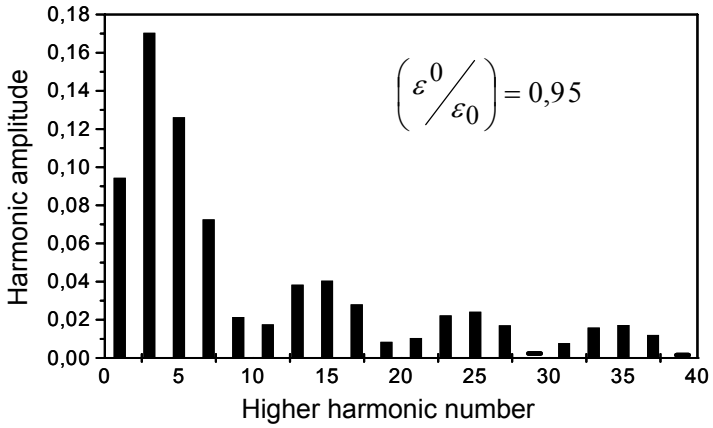

Fig. 6. Sinc-modulated odd higher harmonic CAN spectrum in micro-slip mode.

(for a stick phase) and dynamic values (zero in slide phase) twice over the input strain period according to the following relation:

$$C(t) = (C_S / 2)\{\ 1 - sign(\dot{\varepsilon})sign[\varepsilon + sign(\dot{\varepsilon})\varepsilon_1]\ \}\ . \tag{4}$$

By integrating (4) on strain one obtains σ as a double valued function of ε with the integration constant providing its continuity according to Fig. 7:

$$\sigma(t) = C(t)\varepsilon(t) + C(t)\varepsilon_1 sign(\dot{\varepsilon}) + (C_s / 2)(\varepsilon_0 - \varepsilon_1)sign(\dot{\varepsilon})\,. \tag{5}$$

Since $C(t)$ is a $2\nu_0$-function, none of the terms in (5) contain even-order higher harmonics. The lack of even harmonics is also substantiated by the fully-rectified output waveform to be observed in this case (Fig. 7). The amplitudes of the odd harmonics are found from the spectrum of (5) as follows:

$$\begin{aligned} B_N = C_s\varepsilon_0[\Delta\tau_f\,(\,&sinc\,(N-1)\Delta\tau_f + sinc\,(N+1)\Delta\tau_f - \\ &- 2\Delta\varepsilon\, sinc\, N\Delta\tau_f) - 0.5(1-\Delta\varepsilon)\,\big|\ sinc\, N/2\big|], \end{aligned} \tag{6}$$

where $\Delta\varepsilon = \varepsilon_1 / \varepsilon_0$; $\Delta\tau_f = (1/2\pi)\,Arc\cos(\Delta\varepsilon)$ and $N = 2n+1$ ($n = 0, 1, 2, 3...$).

Spectrum (6) is shown in Fig. 8 and features obvious evidence for the friction dependent *sinc*-modulation.

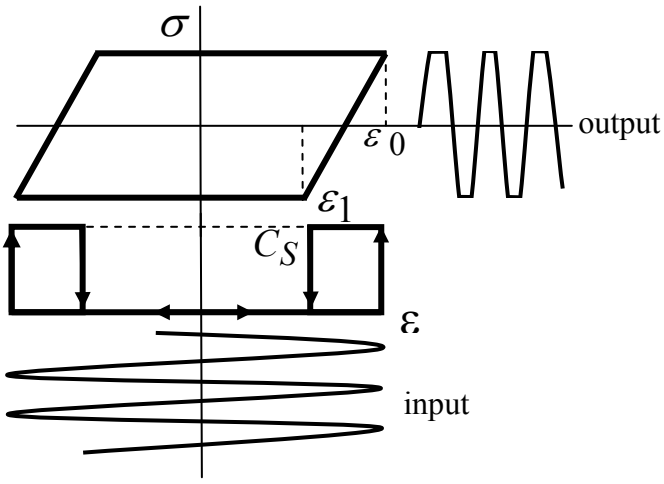

Fig. 7. Stress-strain relation and stiffness variation for sliding friction coupled surfaces in contact.

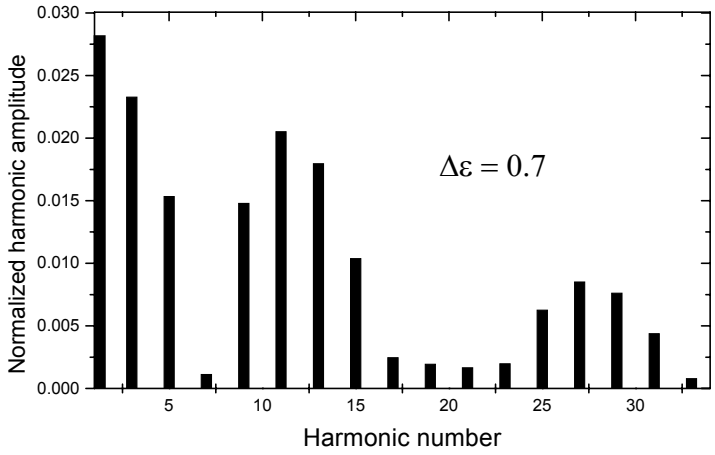

Fig. 8. Odd harmonic CAN spectrum in stick-and-slide mode.

3. Wave mixing via CAN

The higher harmonic generation considered above, results from the "self-modulation" of the contact stiffness driven by an intense acoustic wave. For a dual-wave acoustic excitation, the stiffness modulation leads to mixing of the driving frequencies. The magnitudes of the modulation side-lobes are nonlinear indicators of cracked defects and are used for NDT of their presence in materials. Since CAN is the higher-order nonlinearity the frequency mixing develops very efficiently and includes multiple combination frequency components.

In experiments, the dual-wave drive is usually a combination of an intense low-frequency (pump) and weak higher frequency (probing) acoustic waves:

$$\varepsilon(t) = \varepsilon_{0\nu} \cos \nu t + \varepsilon_{0\Omega} \cos \Omega t \quad , \tag{7}$$

where $\varepsilon_{0\nu} << \varepsilon_{0\Omega}$.

For the pre-strained "clapping" contact introduced above (Fig. 2), the pump wave acts as a switch for the stiffness modulation with frequency Ω (Fig. 9, left):

$$\Delta C_{\Omega}(t) = \Delta C \cdot H\left(\varepsilon_{0\Omega} \cos \Omega t - \varepsilon^{0}\right) . \tag{8}$$

The nonlinear response of the defect at mixing frequencies is thus obtained as follows:

$$\sigma^{MIX}(t) = \Delta C_{\Omega}(t) \cdot \varepsilon_{0\nu} \cos \nu t \quad . \tag{9}$$

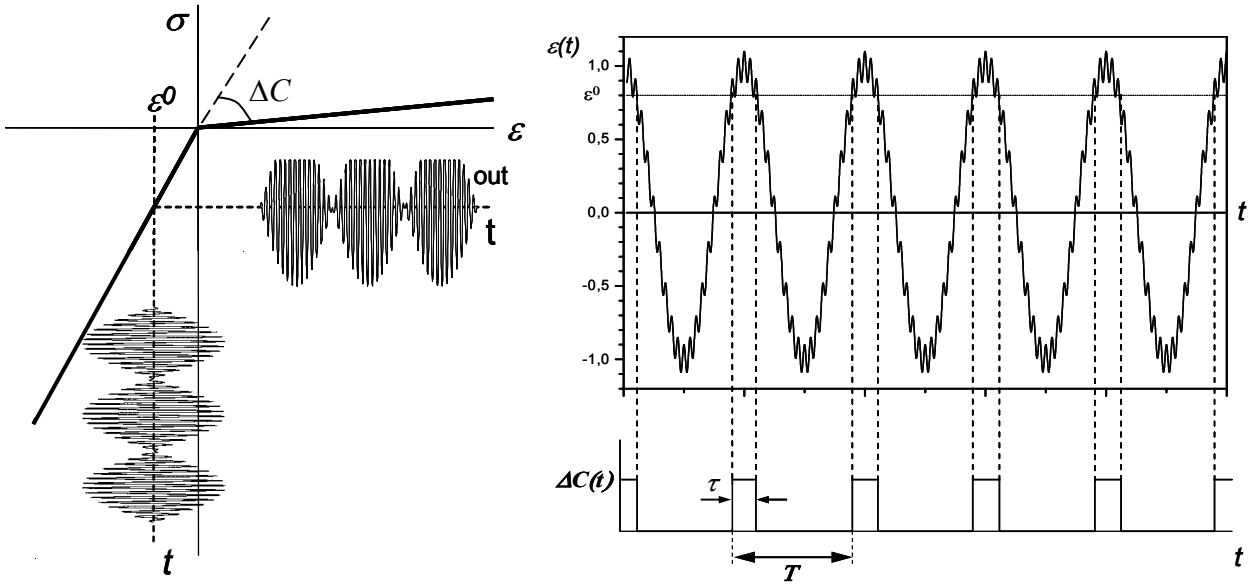

Fig. 9. Mechanical diode model (left) and contact stiffness modulation for dual-wave input (right).

Since the stiffness modulation is a pulse-type function (Fig. 9), the mixing frequency terms in (9) acquire *sinc*-modulation and finally take the form:

$$\sigma^{MIX}(t) = \Delta C \varepsilon_{0\nu} \left(\frac{\tau}{T_\Omega} \right) \sum_{n=1}^{\infty} \mathrm{sinc}\left(\frac{n\tau}{T_\Omega} \right) \left[\cos(n\Omega + \nu) + \cos(n\Omega - \nu) \right] \tag{10}$$

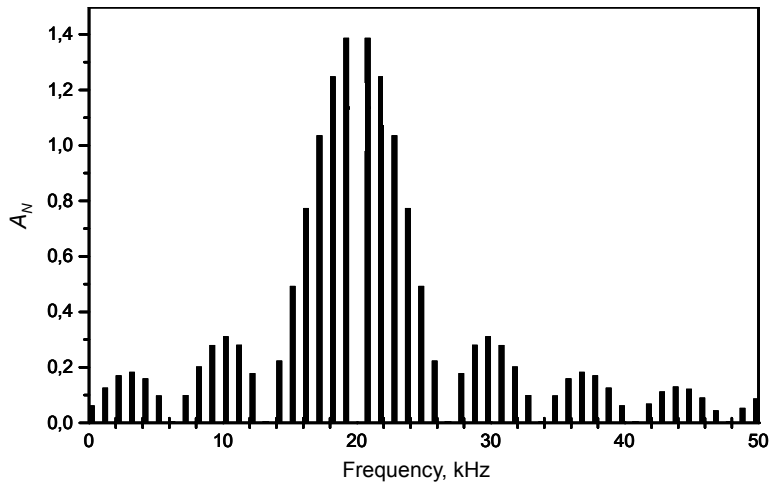

Fig. 10. Calculated CAN frequency mixing spectrum for $\Omega / 2\pi = 1kHz$ $\nu / 2\pi = 20kHz$ and $\varepsilon_{0\Omega} = 10\varepsilon_{0\nu}$.

According to Fig. 10, the frequency mixing spectrum is centred around the high frequency component and comprises multiple combination frequencies with *sinc*-modulated amplitudes.

4. Ultra-subharmonics and ultra-frequency pairs

Besides the higher harmonic generation, the experiments [5, 6] also revealed different scenarios of CAN dynamics which expand considerably nonlinear spectra of cracked defects. These scenarios exhibit the forms of dynamic instability, i.e. an abrupt change of the output for a slight variation of the input parameters. To illustrate the feasibility of the new nonlinear vibration modes and ascertain their basic spectral patterns, we assume that the crack exhibits

both resonance and nonlinear properties and thus is identified as a nonlinear oscillator [5]. Its characteristic frequency (ω_0) is determined by a linear stiffness and an associated mass of the material inside the damaged area (Fig. 11). The contact nonlinearity is introduced as displacement (X) dependent nonlinear interaction force $F^{NL}(X)$. The driven vibrations (driving force $f(t) = f_0 \cos \nu t$) of the nonlinear oscillator are found as a solution to the nonlinear equation:

$$\ddot{X} + \omega_0^2 X = f(t) + F^{NL}(X) \quad . \tag{11}$$

In the second order of the perturbation approach $F^{NL} \sim \cos(\nu - \omega_0)t$ that accounts for the interaction between driving and natural frequency vibrations. If $\nu - \omega_0 \approx \omega_0$, the resonance increase in the output at $\omega_0 \approx \nu/2$ is observed (subharmonic resonance). The higher-order terms in the interaction correspond to the frequency relation $m\nu - n\omega_0$ that provides resonance output at $\omega_0 \approx m\nu/(n+1)$. For $n = 1$, the crack generates ultra-subharmonics (USB) of the second order $m\nu/2$; the higher order USB correspond to the higher values of n.

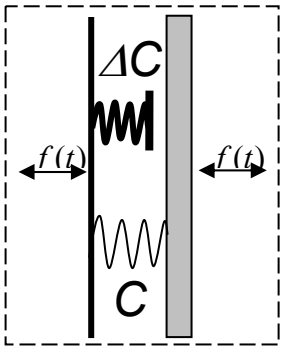

Fig. 11. Resonance model of a clapping crack.

In reality, a damaged area has a more complicated structure that can be conceived as a set of coupled nonlinear oscillators (a pair of those with normal frequencies ω_α and ω_β is shown in Fig. 12). If the frequency of the driving acoustic wave is $\nu \approx \omega_\alpha + \omega_\beta$, the difference frequency components $\nu - \omega_\alpha \approx \omega_\beta$ and $\nu - \omega_\beta \approx \omega_\alpha$ provide cross excitation of the coupled oscillators. It results in a resonant generation of the frequency pair (FP) ω_α, ω_β centred around the subharmonic position.

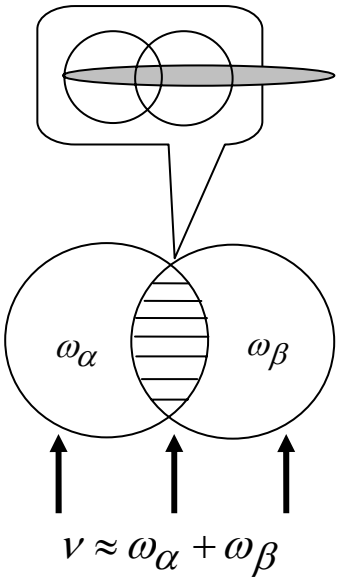

Fig. 12. Crack as a set of coupled nonlinear oscillators.

The resonance increase of the spectral components of combination frequency requires to take into account the higher-order nonlinear terms in the driving force. It opens an opportunity for the combination-type resonance with a larger number of normal modes and also expands the nonlinear spectrum due to the interplay between existing resonant excitations $\omega_{\alpha,\beta}$ and ν. In the latter case, after accounting for the N th-order terms, the spectrum includes the following frequency components:

$$F^{NL}(\omega) \sim \sum_{m,n,p} F_{mnp}(n\nu + m\omega_\alpha + p\omega_\beta), \tag{12}$$

where $m + n + p = N - 1$.

Besides the ultra-harmonics $n\nu$, the nonlinear spectrum in (12) comprises the ultra-frequency pairs (UFP) $(n\nu + m\omega_\alpha + p\omega_\beta)$ and $(n\nu + p\omega_\alpha + m\omega_\beta)$. They are separated by $|m - p|\Delta$ ($\Delta = \omega_\beta - \omega_\alpha$), centered around $[n\nu + (m+p)\nu/2]$ and structured into 2 sets:

1. A set centred around the ultra-subharmonics (USB) $(2a+1)\nu/2$: in this case, $m + p = 2a + 1$ is odd as well as $m - p = [2(a-p)+1]$. Thus, the first UFP components of

the set are shifted by $\pm\Delta/2$ with respect to the USB. If $\omega_\alpha = \omega_\beta$, then the spectrum contains only the higher harmonics ($n\nu$) and USB $(2a+1)\nu/2$.

2. A set centered around integer multiples of ν. In this case, $m+p=2b$ is even as well as ($m-p$) and the UFP series starts at $\pm\Delta$ from the harmonics.

These features of the nonlinear spectrum are shown in Fig. 13 where the results of calculations based on (12) are given for the normalized amplitudes $F_{mnp}=1$ and N=8.

The USB and UFP belong to the class of the instability modes and can be interpreted, respectively, as a half-frequency and combination frequency decay of a high-frequency phonon (driving frequency signal). The resonance growth of these modes is possible only if the input excitation exceeds a certain threshold; it is then affected by the amplitude and frequency instability and hysteresis [7]. The resonance instability manifests in the avalanche-like amplitude growth beyond the input threshold. The reverse amplitude excursion results in bistability: the input amplitudes for the up and down transitions are different (amplitude hysteresis). Such a dynamics is a distinctive signature of the nonlinear acoustic phenomena associated with nonlinear resonance.

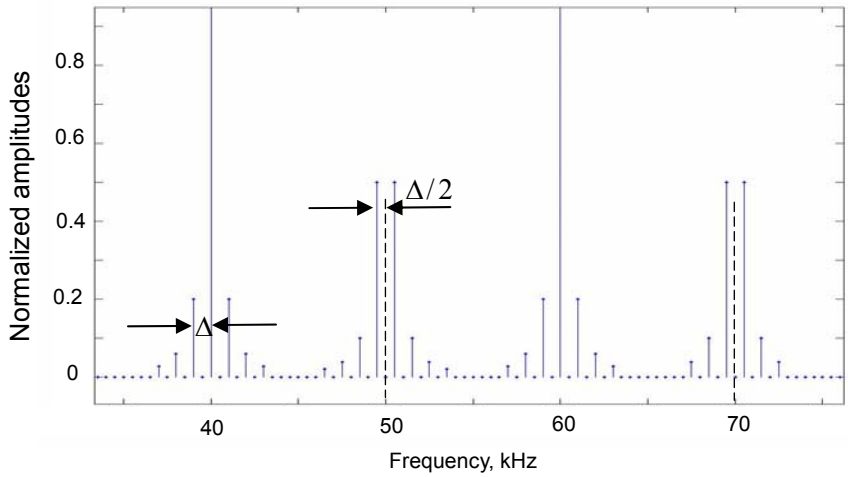

Fig. 13. Section of calculated UFP spectrum: $\nu = 20$ kHz; $\omega_\alpha = 9$ kHz; $\omega_\beta = 11$ kHz; $N = 8$;

5. Experimental observations of nonlinear spectra of defects

5.1 Higher harmonics and frequency mixing

To observe the vibration spectra of defects the laser scanning vibrometry was adapted for nonlinear measurements (nonlinear scanning laser vibrometry (NSLV) [8], Fig. 14). A piezo-stack transducer connected to CW high-power Branson PG generator was used for generation of intense ultrasonic waves (frequencies 20 and 40 kHz, strain amplitudes up to ~10^{-3}). For plate-like specimens studied, it excites flexural waves whose out-of-plane particle velocity induces frequency modulation of the laser light reflected from the surface of the specimen. After demodulation in the controller OFV 3001S of Polytec scanning vibrometer PSV 300 and A/D conversion, the spectrum of the vibrations (particle velocity output) is obtained over 1 MHz bandwidth by FFT in the PC-unit (Fig. 14).

Fig. 15 shows the vibration spectra measured in a cracked carbon fibre-reinforced plastic (CFRP) specimen. In the intact region, the driving frequency (20 kHz) dominates in the vibration spectrum (Fig. 15, top). The second harmonic content amounts to a few percent with

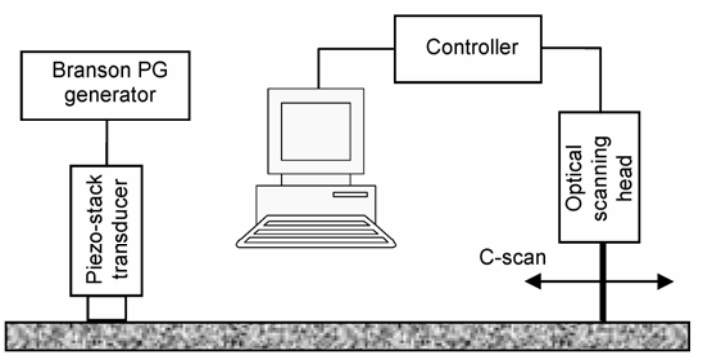

Fig. 14. Experimental setup for NSLV.

a minor indication of the higher harmonics. In the cracked area (Fig. 15, bottom), the spectrum reveals extremely efficient generation of multiple higher harmonics: their amplitudes are comparable to that of the driving frequency with evident indication of the *sinc*-modulation envisaged in section 2. The anomalously high local increase of the higher harmonics in the damaged areas makes the CAN based NDT much less critical to the spurious signals than its classical counterpart. A few percent klirrfactor is admissible for the signal generators; no strict requirements are imposed on the transducer monochromaticity and filtering circuits.

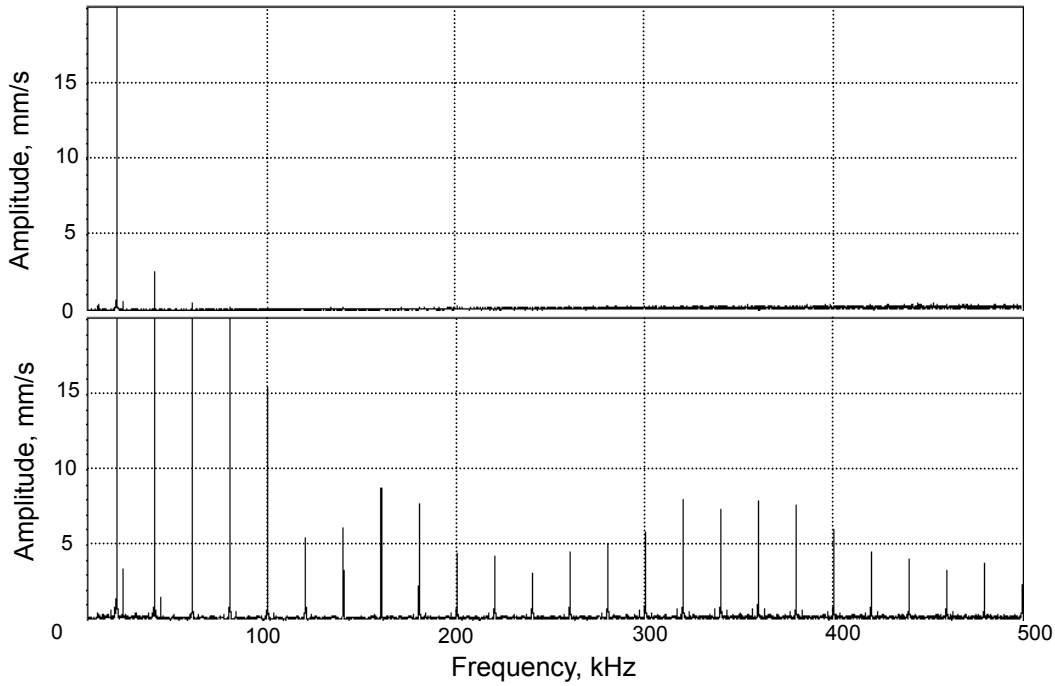

Fig. 15. Vibration spectra of cracked carbon fibre reinforced specimen measured outside (top) and inside the damage area (bottom); excitation frequency is 20 kHz.

The mechanism of friction nonlinearity which according to section 2.2 is supposed to provide only odd harmonic generation was found to prevail in wood which is a natural fibre-reinforced composite. In intact wood, the higher harmonic spectrum averaged over the specimen surface exhibits an evident odd harmonic domination (Fig. 16, left). Then the specimen was damaged (crack made by cutting) and the spectrum measured in the neighbourhood of the crack acquires even higher harmonics (Fig. 16, right) obviously generated due contact clapping in the crack. The change of type nonlinearity enables to use the harmonic signature for discerning and imaging flaws in wood and wood composites.

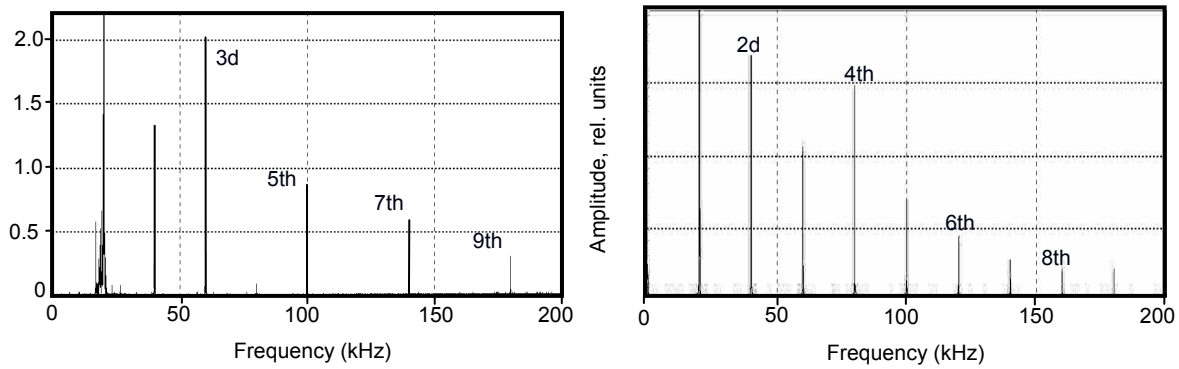

Fig. 16. Odd (left) and odd/even (right) higher harmonic spectrum in intact and damaged wood specimen driven at 20 kHz.

The results of the frequency mixing experiment via CAN are shown in Fig. 17 for a delamination on the top of a piezo-actuator embedded into a glass fibre-reinforced composite (GFRP). Such "smart" sensors are being used for structural health monitoring of aerospace components using plate ultrasonic waves. The actuator was used for excitation of high-frequency probing ($\nu/2\pi = 388$ kHz) plate waves while intense low-frequency ($\Omega/2\pi = 15$ kHz) pump drive was applied to the specimen to produce stiffness modulation in the defect area.

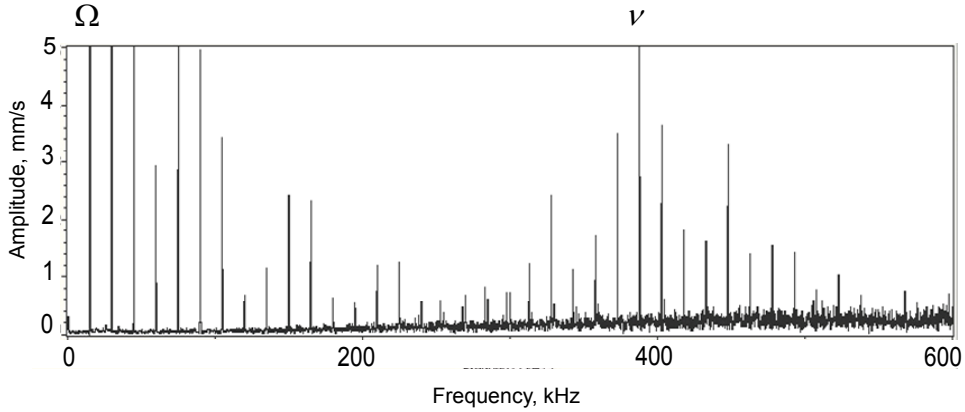

Fig. 17. Frequency mixing spectrum in delamination area in GFRP specimen: probe wave frequency is 388 kHz; pump wave frequency – 15 kHz.

Fig. 17 shows that the nonlinear spectrum includes the higher harmonics of the pump frequency (left hand side part) and the mixing frequency components (grouped around the probing frequency). In accord with sections 2 and 3, both parts of the spectrum reveal *sinc*-type modulation; the mixing frequency part of the spectrum agrees well with the calculations presented in Fig. 10.

A specific feature of the clapping CAN mechanism is concerned with nonlinear rectification of the output signal which manifests in both the higher harmonic (Fig. 2) and frequency mixing (Fig. 9) cases. The experimental evidence for the nonlinear distortion of the vibrations obtained in the weakly-bonded contact area between alloyed metals in an engine block is illustrated in Fig. 18. The component was driven by two pump ultrasonic waves of approximately equal amplitudes with frequencies of 19.5 and 20.5 kHz. Their combination produced a sinusoidally modulated excitation in the form of 1 kHz frequency beatings. The output frequency beating signal in the defect area is found to be heavily rectified (Fig. 18) which agrees fully with the mechanical diode phenomenology (see Fig. 9, left).

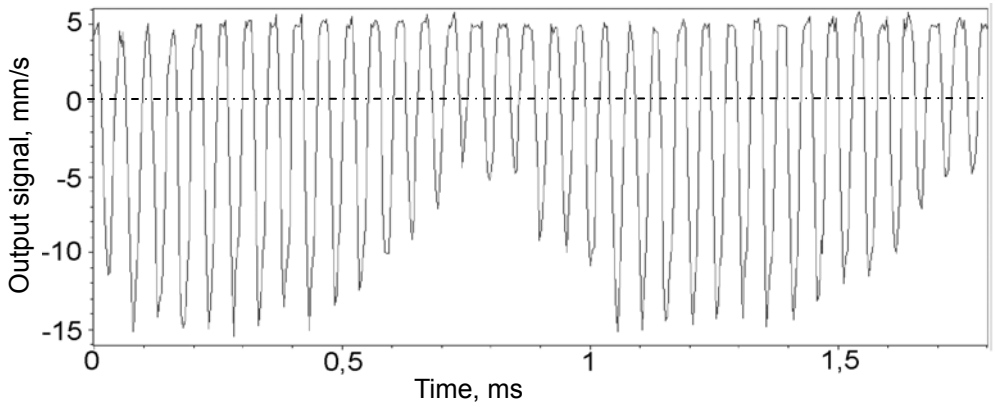

Fig. 18. Nonlinear rectification of vibrations for dual-frequency excitation of a weakly-bonded contact.

5.2 Observation of ultra-subharmonic and ultra-frequency pair spectra

Unlike the higher harmonics, the USB-UFP frequencies are barely produced in the generator/transducer system and define virtually zero background level outside the defect areas. To this end, such spectra were found to be more advantageous for the nonlinear NDT and imaging. The examples of the USB and UFP spectra observed in damaged materials are shown in Figs. 19-24.

The USB-spectra in Fig. 19 are measured in a cracked area of carbon-fibre reinforced plastic (CFRP) rod (8x25x350 *mm*) driven by 40 kHz excitation. For a low-level drive, the spectrum consists of only higher harmonics of the driving frequency (Fig. 19, top). The higher harmonic pattern changes abruptly for the USB spectrum (period doubling bifurcation) as the driving amplitude grows beyond a certain threshold value. The resonance enhancement of the ultra-subharmonics combined with their contribution to the higher harmonics changes dramatically overall nonlinear spectrum (Fig. 19, bottom). The "wavy" amplitude modulation of the spectral lines indicates involvement of the CAN mechanisms into USB generation.

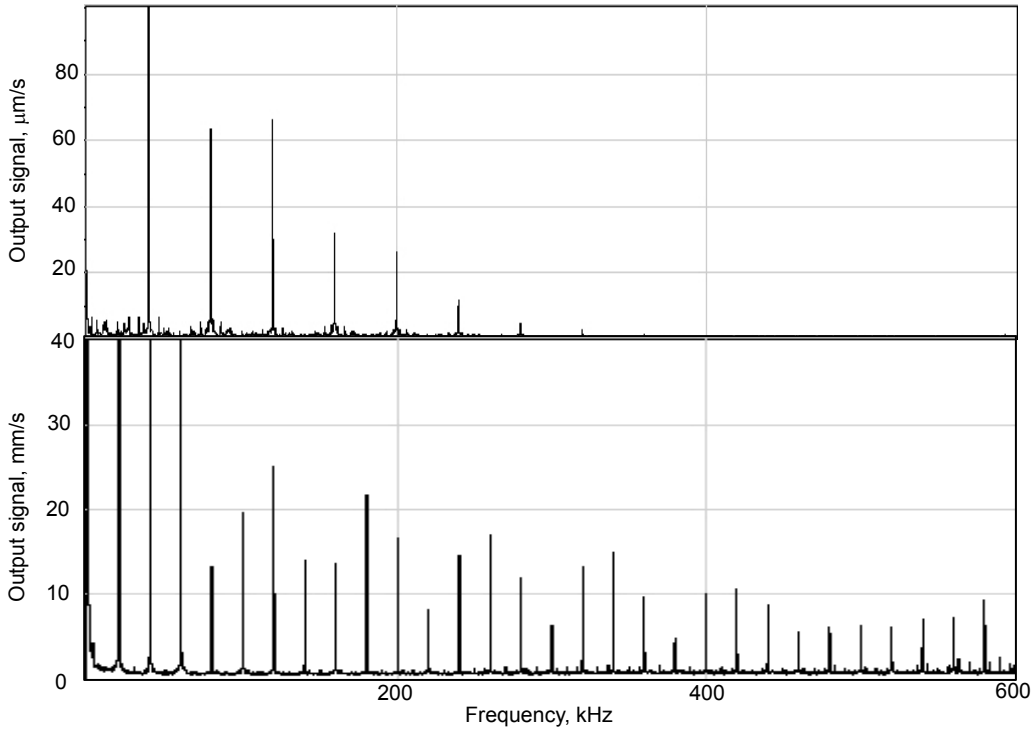

Fig. 19. Bifurcation of the higher harmonic spectrum (top) into USB (bottom) in damaged CFRP specimen.

The zoom-in sections of the nonlinear spectra observed for further increase of the input signal are shown in Fig. 20. It illustrates the bifurcation of the second order USB into the higher order ultra-subharmonic spectrum. According to section 4, such a spectrum comprises the fractional components of the driving frequency $m\nu/(n+1)$. The pattern shown in Fig. 20, top corresponds to $n=10$ that provides the USB frequencies multiples of $\nu/11 \approx 3.6$ kHz. Further increase of the input causes successive decay of the USB frequencies (Fig. 20, bottom) into the higher-order USB ($n=12$ in Fig. 20, bottom). Such a cascade sequence of bifurcations eventually results in a quasi-continuous spectrum characteristic of chaotic vibrations.

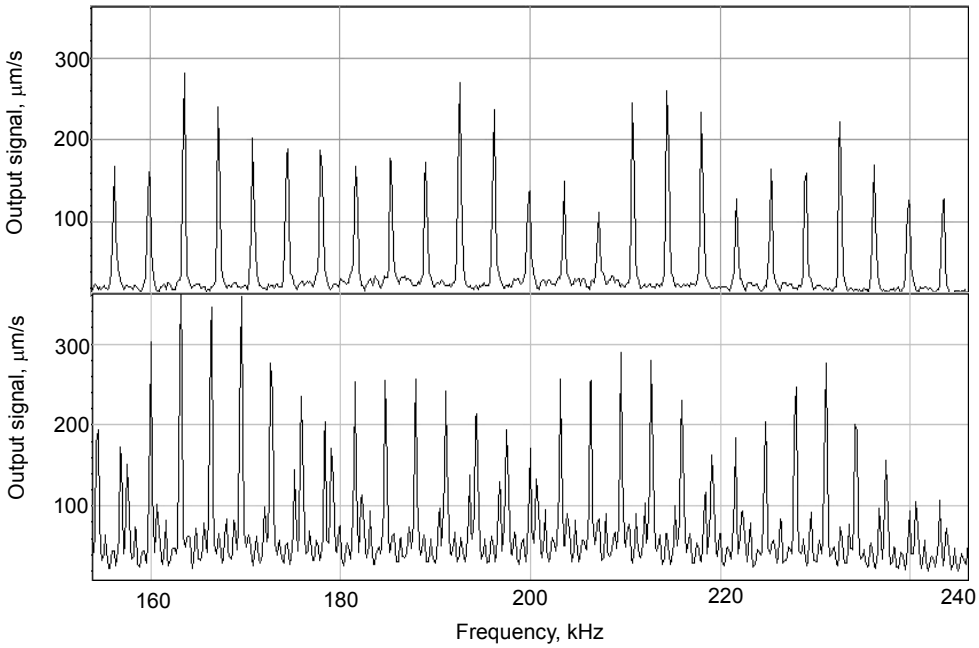

Fig. 20. Cascade USB bifurcation in damaged CFRP rod: 11th-order USB (top); 13th-order USB (bottom).

The dynamic properties of the USB modes are illustrated in Fig. 21. The figure shows the amplitude of $3\omega/2$-subharmonic wave generated in the reflection of 30-MHz acoustic waves from a crack in $LiNbO_3$ crystal [9], as a function of the input voltage. One can clearly see the step-wise thresholds ($(V_{IN})_1 \geq 3V$; $(V_{IN})_2 \geq 4V$) followed by the stable plateaus. The sharp increase at the thresholds confirms a transition into the instability region where the avalanche-like development of nonlinear oscillations takes place. The hysteresis of the curves in Fig. 21 is the evidence of bistability in the crack signature [9].

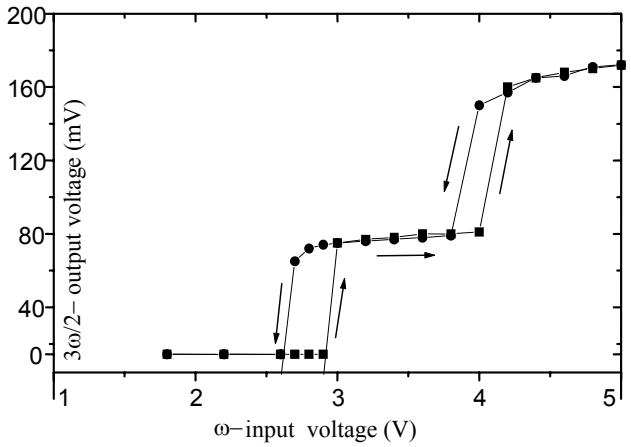

Fig. 21. Dynamic threshold and bistability of USB mode.

As was mentioned in section 4, realistic damage defects often have a complicated structure and might display multi-frequency nonlinear resonances leading to the UFP generation. Such behaviour is illustrated in Fig. 22 which shows the nonlinear vibration spectra measured in different parts of an extended (few cm) delamination area in GFR-concrete slab. A classical FP doublet with $\Delta \approx 3$ kHz (top) corresponds to the vibration mode represented by a pair of coupled nonlinear oscillators (section 4). A more complicated pattern in an adjacent area results in a two-pair local FP spectrum (middle).

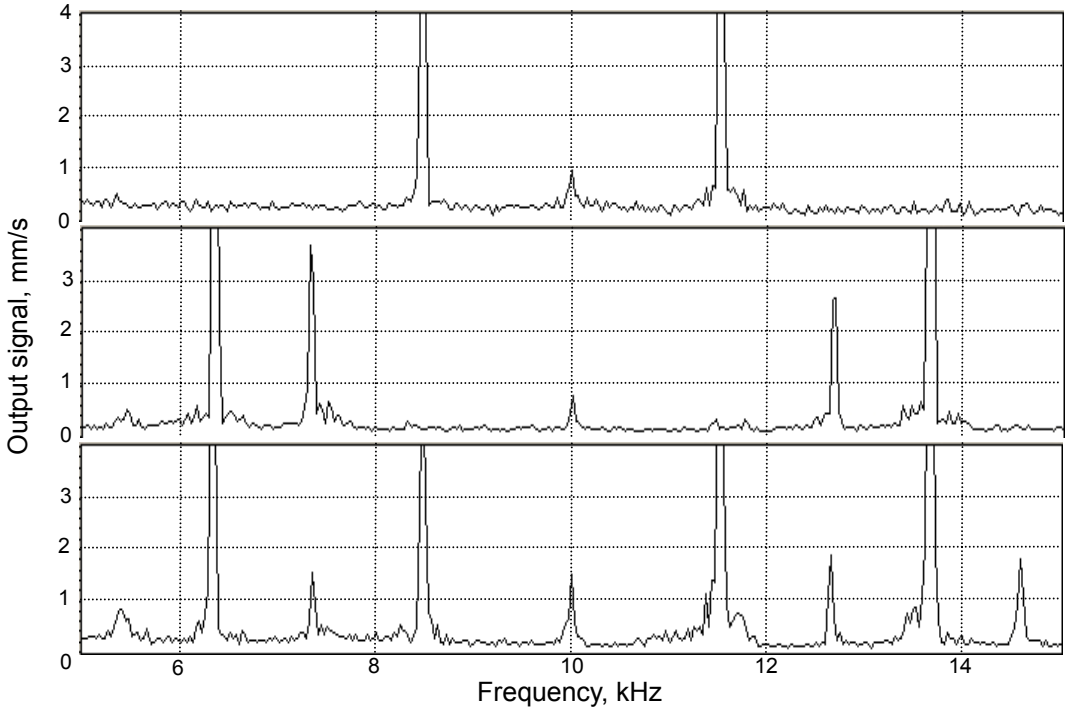

Fig. 22. Frequency pair spectrum in different parts of delamination in GFR-concrete slab; excitation frequency is 20 kHz.

Elastic coupling between the two parts of the same delamination provides the FP spectrum which is a combination of the above (Fig. 22, bottom).

A good agreement between experimental observations and the nonlinear resonance approach of section 4 is also seen in Fig. 23 which shows a section of the UFP spectrum measured in the impact damage area of GFRP composite for a 20-kHz (ν) excitation. One can identify the positions of the second (40 kHz) and third (60 kHz) harmonics as well as ultra-subharmonics (50 & 70 kHz). The UFP lines are centred around the USB positions and distanced from them by $\Delta/2 \cong 0.6$ kHz (see UFP set 1, section 4). As expected, the UFP around higher harmonics reveal twice larger shift $\Delta \approx 1.2$ kHz (UFP set 2, section 4). Overall agreement between the theory and experiment is evident by comparison of Fig. 13 and 23. It is worth noting again, that the UFP signals are observed exclusively in the impact area and are not produced in the excitation system.

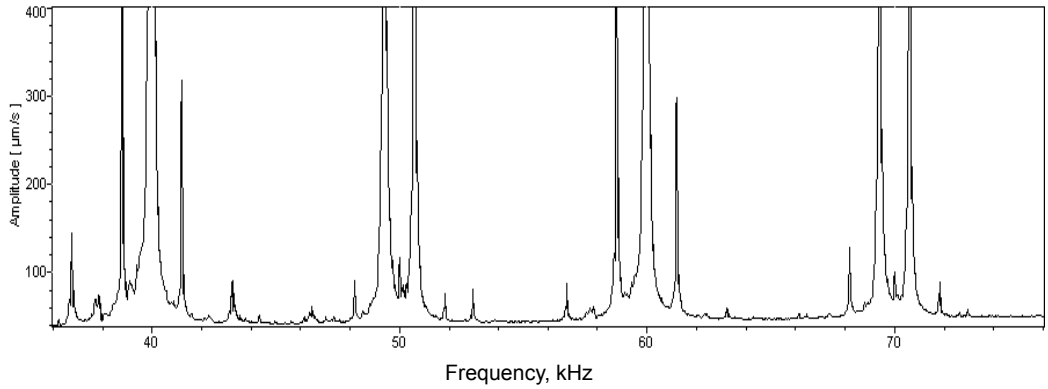

Fig. 23. A section of UFP spectrum in impact damage area of GFRP specimen; excitation frequency is 20 kHz.

Similar to the USB modes, the resonance growth of the UFP components is observed only if the input excitation exceeds a certain threshold and is affected by the amplitude and frequency instability and hysteresis. Fig. 24 provides direct evidence for the spectral transformations

beyond the subharmonic instability threshold for a delamination area in a C/C-SiC-composite. As the driving amplitude of the 20-kHz excitation exceeds the threshold for the subharmonic mode (≈ 0.5 μm in Fig. 24), another instability threshold gives rise to a bifurcation into the UFP-components (at ≈ 1μm-drive). The oscilloscope insert in Fig. 24 illustrates the self-modulation of the output signal in the damaged area accompanying the USB-UFP transition. A further increase of the input results in widening of the UFP-lines into quasi-continuous frequency bands which are the forerunners of the transition to chaos.

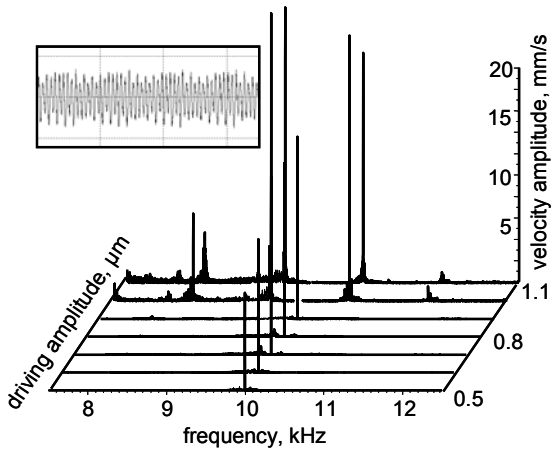

Fig. 24. USB-UFP bifurcation in delamination area of C/C-SiC-composite

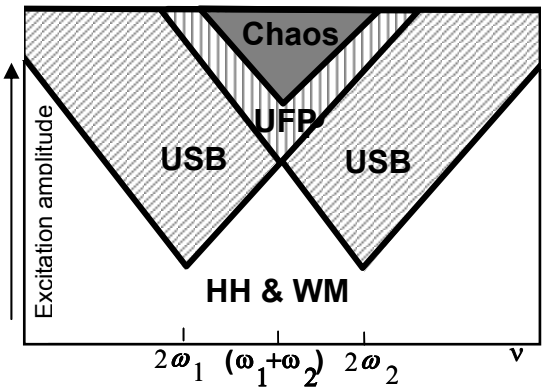

Fig. 25. Schematic diagram of nonlinear dynamics for a cracked defect represented as a pair of coupled nonlinear oscillators.

The experimental results on the nonlinear dynamics of fractured flaws are summarized schematically in Fig. 25 for a defect represented by a pair of coupled oscillators (normal frequencies ω_1 and ω_2). At low amplitude of the driving excitation (strain amplitudes $\varepsilon \approx (10^{-6} - 10^{-5})$), the nonlinear spectrum follows the non-resonant scenario of the higher harmonic and the wave mixing (sections 2, 3). As the input amplitude exceeds the threshold value ($\varepsilon \approx (10^{-5} - 10^{-4})$), resonance instability generally results in the activation of the USB components first. The threshold amplitude depends on the driving frequency: a minimal threshold requires frequency matching to the subharmonic resonance ($\nu = 2\omega$) (Fig. 25).

The frequency zones for the USB generation expand readily as the excitation amplitude increases. Further increase of acoustic excitation above a given threshold gives rise to the UFP spectra. A direct transition from the non-resonance modes to the UFP-instability is also possible when the sum-frequency resonance matching conditions are satisfied. The *V*-shaped zones in Fig. 25 are typical for nonlinear resonance phenomena as shown by numerical calculations using parametric approach to nonlinear resonance [7]; they were also observed in our experiments [10]. It means that for high driving amplitudes the frequency matching is not required and both USB and UFP modes can be observed virtually independent of the input frequency. Finally, the multiple UFP bring the system to a quasi-continuous spectrum which indicates a build-up of chaotic vibrations.

6. Case studies of NNDT

6.1 NSLV for defect-selective imaging

The nonlinear spectra discussed above are produced locally in the damaged area while an intact part of material outside the defects vibrates linearly, i.e. with no frequency variation in the output spectrum. This makes nonlinearity a ***defect-selective*** indicator of damage presence and development. The high localization of nonlinear spectral components around the origin is a basis for nonlinear imaging of damage.

For this purpose, a spectral line is selected from the nonlinear spectrum detected by the laser vibrometer after a C-scan and the distribution of this component over the specimen surface is presented as a colour-coded image. Since all nonlinear contributions to the vibration spectrum are generated locally in the flaw area, any of those frequencies can be used for defect location and imaging. As a result, for a fixed input frequency, a single C-scan yields a number of images of the defect corresponding to various output spectral components. This is another apparent benefit of the NNDT which enhances the probability of the flaw detection. Usually the nonlinear images at different frequencies are closely related but not identical because the optimal conditions for generation of different nonlinear components vary over the defect area. In what follows, the selection of particular frequencies for nonlinear imaging is based on the best signal-to-noise ratio to provide at least (10-20) dB difference between the nonlinear response of the defect and the outside background.

6.1.1 Higher harmonic and frequency mixing imaging

Higher harmonics in damaged materials are readily generated at reasonably small input amplitudes (strain ~ 10^{-7}- 10^{-6}), so that even internal or other low-amplitude vibration sources provide enough energy for the higher harmonic imaging.

The internal excitation activates clapping mechanism of higher harmonic generation in a number of mechanical units which use gear boxes and push-pull components. In many cases, the presence of clapping may indicate a faulty part of an instrument. Fig. 26 illustrates a feasibility of detection of the clapping components in a commercial saw-cutting tool. The 3d harmonic image of the motor rotation frequency clearly locates position of the worm-gear transmission (Fig. 26, right) which moves in a nonlinear (clapping) way.

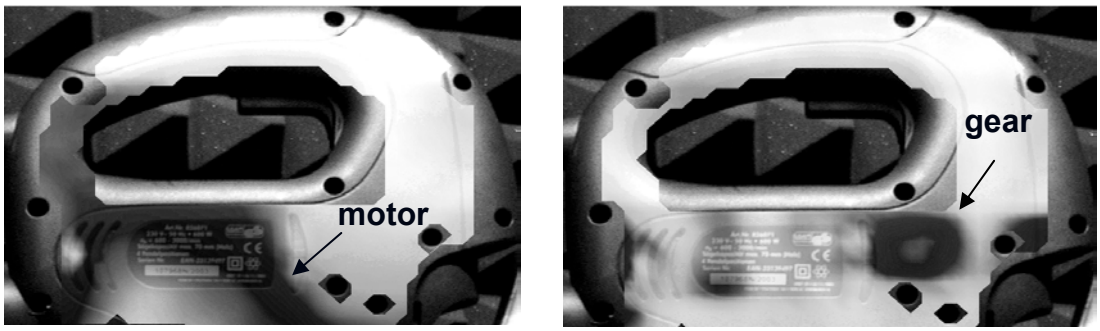

Fig. 26. Linear (left) and third harmonic (right) NSLV-images of saw-cutting tool.

Another example demonstrating the defect-selective character of the nonlinear imaging is shown in Fig. 27. The fundamental frequency (20 kHz) NSLV image of the damaged area in fabric carbon-kevlar fibre-reinforced composite (left) reveals a pronounced standing wave pattern in the specimen with no indication of damage. The higher harmonic images (Fig. 27, middle and right) selectively indicate the point impact damage. The signal-to-noise (background standing wave) ratio of the nonlinear images is about 20 dB for the 3d harmonic in Fig. 27. It usually increases for the higher-order nonlinear frequency components since their level is lower in the excitation source.

The use of the higher-order harmonics is particularly important in the low-dissipative materials like, metals where standing wave interference is especially disturbing. This advantage is illustrated in Fig. 28 for a dog-bone shaped Al cylinder of 30/20 mm diameter with fatigue crack. A noticeable decrease in the background standing wave is seen as the order of the higher harmonic images increases from 4 to 16.

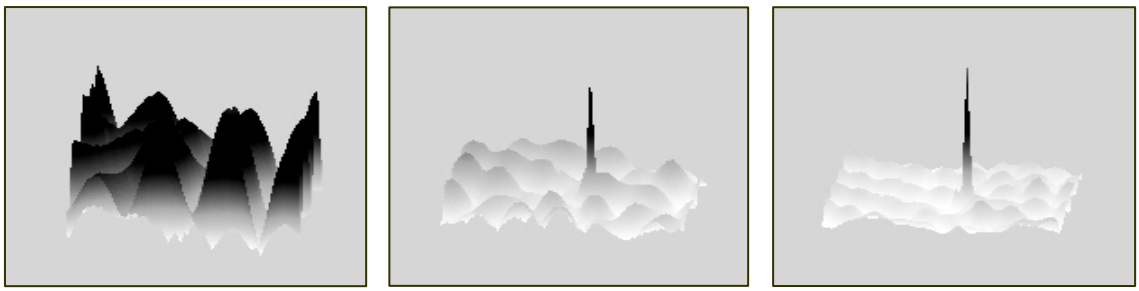

Fig. 27. Linear (left), second (middle) and third harmonic (right) NSLV-images of a point impact damage in carbon-kevlar composite.

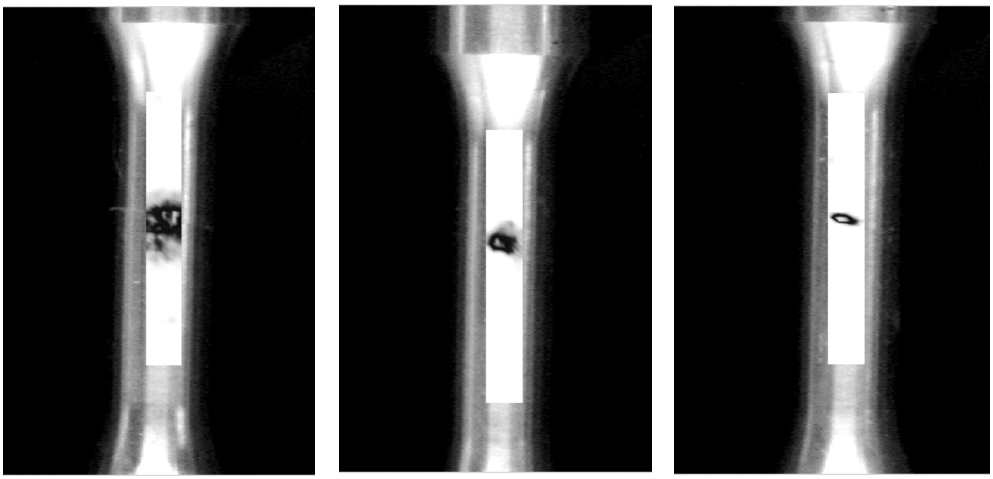

Fig. 28. NSLV-imaging of fatigue crack in AL cylinder: 4^{th} (left), 9^{th} (middle) and 16^{th} harmonic images.

Due to a relatively moderate input power required, a flexible operation in the higher harmonic mode can be achieved even for large industrial parts by using portable ultrasonic transducers. An example in Fig. 29 shows nonlinear imaging of a fatigue crack in a riveted aviation component. The 20-kHz excitation was implemented with "dry-contact" portable piezoelectric transducers attached to the specimen by vacuum suction. The use of a pair of transducers enabled to obtain a more homogeneous driving ultrasonic field and thus to reduce the influence of the standing waves.

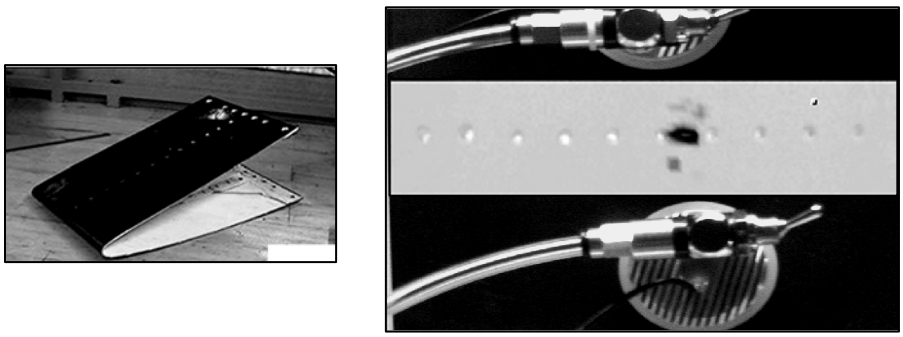

Fig. 29. Higher harmonic imaging of a fatigue crack in aviation component (left): excitation with portable ultrasonic transducers (right).

The effect of the input signal amplitude is illustrated in Fig. 30 for a multi-ply CFRP- sample (15x20 cm) which has an impact in the middle part and a number of edge delaminations. The 10^{th} harmonic distribution clearly indicates the positions of all defects; the number of delaminations discerned and the image contrast increase substantially for the higher input.

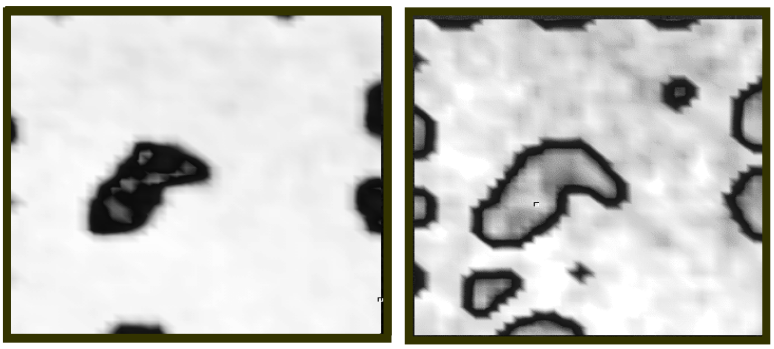

Fig. 30. Tenth harmonic images of defects in CFRP plate for different input amplitudes: strain $\varepsilon \approx 5 \cdot 10^{-5}$ (left) and $\varepsilon \approx 10^{-4}$ (right).

To verify a feasibility of nonlinear imaging of sub-surface defects, a series of edge delaminations embedded in a fabric CFRP plate at different depths was measured (Fig. 31). The four sub-surface delaminations visualized in Fig. 31 (left) are positioned at depths ≈ 0.3; 0.6; 0.9, and 1.2 mm below the surface. The plot of the image contrast (right) indicates substantial decrease in the amplitude of nonlinear surface vibrations as the defect depth increases. A certain improvement in detection of the deep-lying defects was found to be possible by attaching the driving transducer closer to the defect location. In any case, the mm-range of the sub-surface operation seems reasonable for NDT of sheet-like materials typical for aviation and automotive applications.

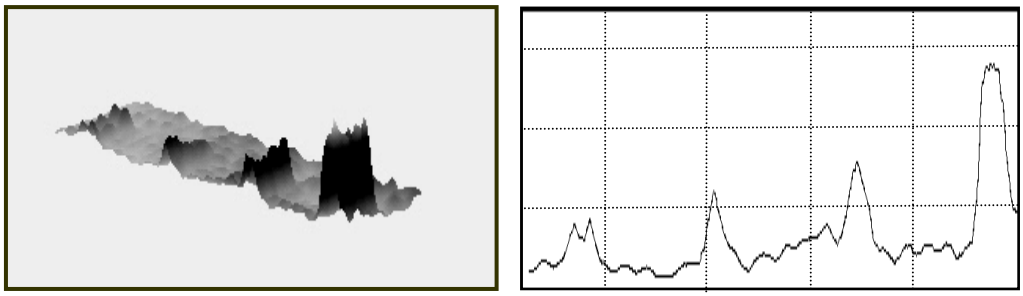

Fig. 31. Fourth harmonic image of 4 sub-surface edge delaminations embedded at different depths in CFRP plate (left); plot of the image contrast (right).

Since a certain level of spurious higher harmonics is inevitable in nonlinear experiments, the wave mixing mode might be advantageous in some applications. Fig. 32 illustrates a case study of nonlinear imaging via frequency mixing in aircraft component (CFRP landing flap for A 330 (left)) with a stringer debond on reverse side. The dual-frequency excitation used a pump 20 kHz wave and a probing 3.3 kHz signal. As the second harmonic image (40 kHz) suffers a strong background noise (Fig. 32, left), the sum-frequency image (right) clearly detects the defect position.

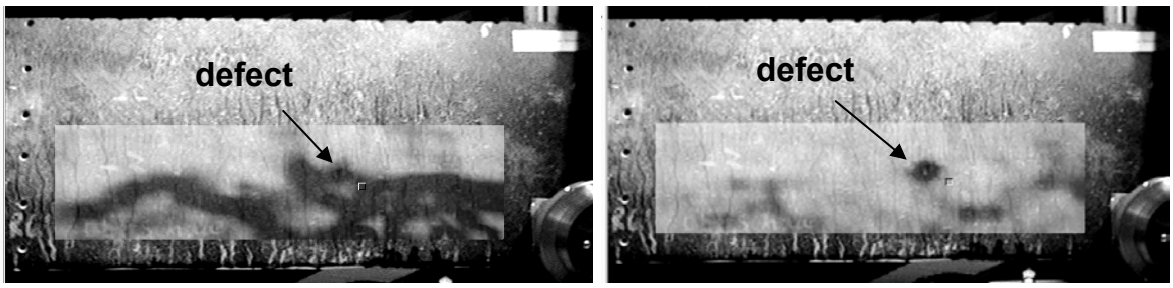

Fig. 32. Nonlinear imaging of stringer debond on reverse side of CFRP aircraft landing flap: second harmonic image (left); mixing frequency image (right).

6.1.2 Nonlinear NDT via USB and UFP

The input acoustic power for the USB- and UFP-modes is somewhat higher than that for the higher harmonic/mixing experiments. In practical terms, this requires an acoustic intensity of a few W/cm^2 in the high-MHz-frequency range and the driving amplitudes of μm-scale in the kHz range. Our experiments also show that the threshold input for the instability bifurcations to occur depends on the degree of material damage.

This fact is illustrated in Figs. 33 and 34 where the zoom-in pictures in the USB threshold areas are given. The specimen measured in Fig. 33 was PMMA plate with different number of surface minute cracks (crazes) changing from few (stage 1) to dozens of cracks (stage 3). The crazes were activated by a drop of acetone and produced by three-point bending of the specimen. It is seen that the minimum USB threshold is observed for the highest damaged induced (stage 3).

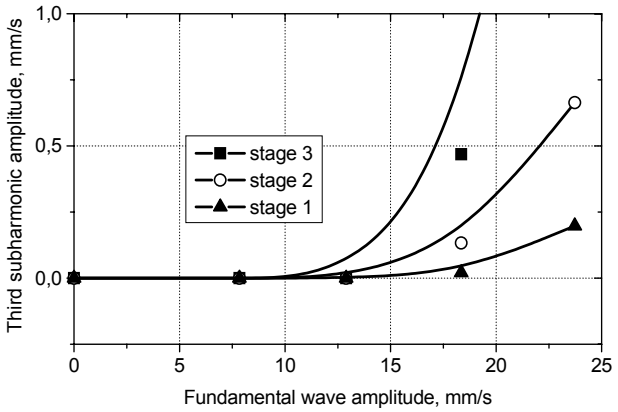

Fig. 33. Zoom-in threshold dynamics in PMMA with different number of crazes.

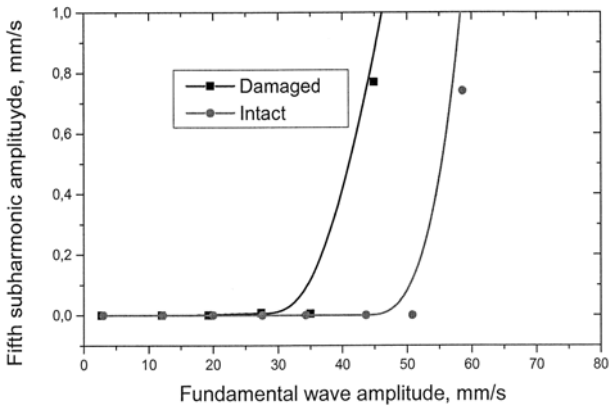

Fig. 34. Threshold dynamics in intact and fatigue damaged multi-layered GF-fabric composite.

Fig. 34 presents similar measurements for intact and fatigue-damaged specimens of multi-layered GF-fabric composite. The almost twofold shift of the USB threshold observed for the damaged specimen indicates that this effect can be applied for overall evaluation of damage in pass/non-pass NDT.

A strong increase of the instability modes beyond the threshold leads to distinctive nonlinear spectra with multiple USB- and UFP-components located exclusively in damaged areas. A few examples of nonlinear imaging of localized defects are given below to demonstrate their applicability and superior performance in the cases where the data obtained by non-resonant (higher harmonics and frequency mixing) modes are insufficient.

Fatigue loads in metals (rotors, turbines, etc.) cause minute cracks of micro-meter scale which gradually develop into major cracking and initiate an abrupt material fracture. The linear ultrasound is virtually unable to detect the fatigued crack at the early stage of their development. Examples of nonlinear imaging of fatigue induced micro-flaws and degradation of metal micro-structure using the USB-modes are given in Figs. 35 and 36.

Fig. 35 shows fatigue cracking produced by cyclic loading in Ni-base super-alloy. Such a crack of ~ 1.5 mm length, with average distance between the edges of only $\approx 5\mu m$, is clearly detected in the USB-image $(7\nu/2)$, whereas traditional linear NDT by using slanted ultrasonic reflection failed to work with such small cracks.

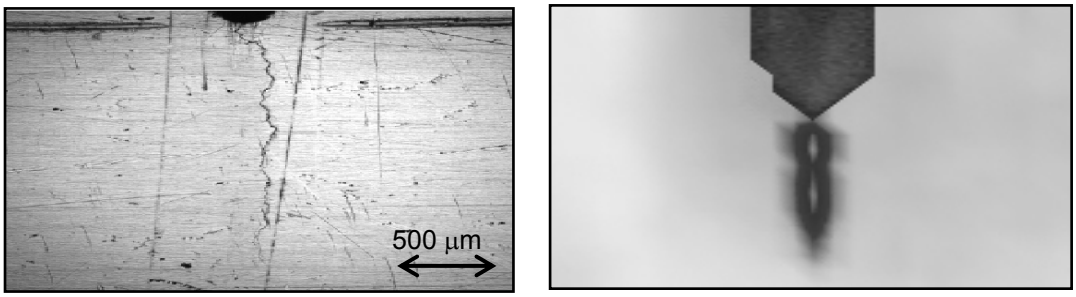

Fig. 35. Right: USB-image of 5μm-wide fatigue crack in Ni-base super-alloy; left: crack photo.

Plastic deformation is known to change the metal micro-structure by generating clusters of dislocations which are the forerunners of micro-cracking. The feasibility of NNDE for such delicate defects in the USB-mode is illustrated in Fig. 36 for a steel auto-component (diameter 0.8 cm; length 6.5 cm) subject to 6% tensile deformation. Some necking initiated in its central part indicates that the plastic deformation was mostly concentrated in its central part. The nonlinear image reveals the area of deteriorated material properties by an evident increase in the USB amplitude.

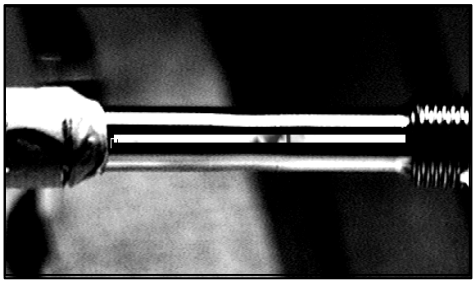

Fig. 36. USB-image of plastic deformation area in a steel component.

Fibre reinforced composites constitute a class of hi-tech engineering materials whose application area is rapidly expanding in aerospace and automotive industries. Fibre metal laminates are new materials with excellent tolerance to impact, corrosion and lightning stroke, low flammability and low weight. Fig. 37 displays an example of NNDE of such an advanced material for aircraft industry: glass fibre reinforced aluminium laminate (Glare®). More specifically, it shows the USB-images of a Glare® plate with two inserted circular Teflon-foils to simulate local delaminations. In the images, the defect can be recognized fairly well, and the quality is enhanced for the higher orders of the USB. We believe that the latter is associated with the peculiar distribution of subharmonics over the delamination area and stronger acoustic dissipation outside the defect at higher frequencies.

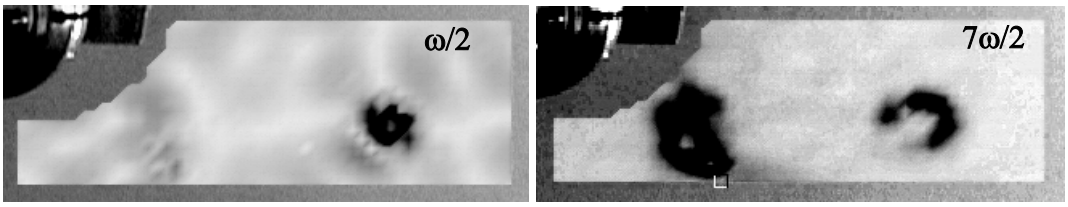

Fig. 37. USB-images of a pair of artificial delaminations in a Glare® plate.

Mechanical impacts in multi-ply composites produce a fracture which is a combination of matrix-fibre debonding, cracking and delaminations. Such a combination of fractured defects makes the impact area strongly nonlinear and, normally, all nonlinear modes can be traced in the spectra observed.

Similarly to all nonlinear modes discussed, the UFP-components generally display a strong spatial localization around the defects and are applicable for the detection of damage. The benefit of the UFP-mode is illustrated in Fig. 38 for a 14-ply epoxy based glass-fiber

reinforced composite (GFRP) with a 9.5J-impact damage. The linear image taken at the driving frequency of 20 kHz reveals only a developed standing wave pattern over the whole sample (Fig. 38, left). The higher harmonic image is also corrupted by the standing wave pattern (centre), whereas the image at the first UFP-side-lobe of the 10^{th} harmonic of the driving frequency (198.8 kHz) yields a clear indication of the damaged area (Fig. 38, right).

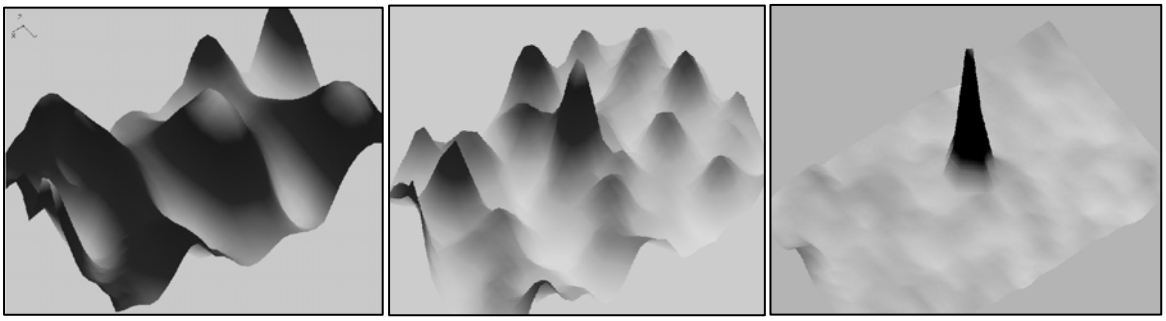

Fig. 38. Nonlinear imaging of impact damage in GFRP: left - linear (20 kHz-image); centre – 5^{th} harmonic image; right - UFP – image.

Two examples of nonlinear monitoring of macro-defects in constructional materials are shown in Fig. 39 for a slab of GFR-concrete (15x30x1.5 cm). Production technology of this material often suffers from cracks and internal delaminations induced by fibre-matrix debonding. Due to a grainy structure of the fragile material, these defects include multi-contact interfaces which are highly nonlinear. It is worth noting, that the grainy structure of

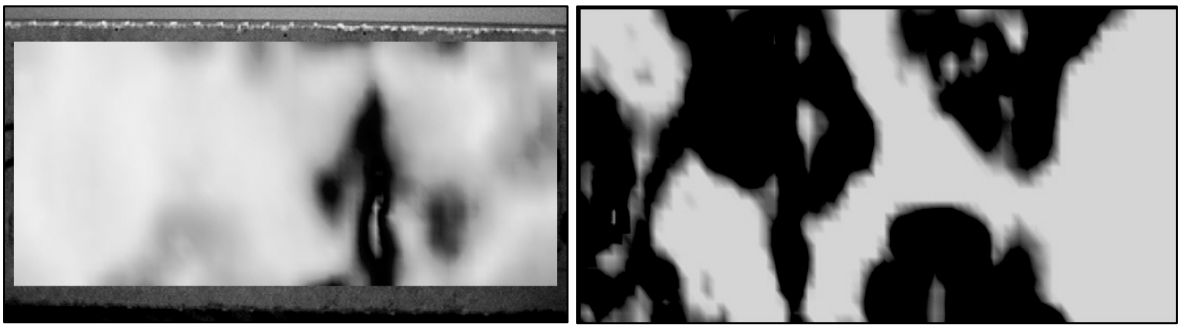

Fig. 39. NSLV imaging in GFR-concrete: USB-image of a crack (left) and UFP(30.5 kHz)-image of delamination area (dark) in GFR-concrete slab (right).

concrete also provides substantial nonlinear response of intact material. Nevertheless, the USB image in Fig. 39, left clearly visualizes a vertical surface crack. A few cm delamination areas in the material should be considered as complicated defects with a set of characteristic frequencies introduced in section 4. Accordingly, an efficient multiple UFP generation was measured in these areas for intense 20 kHz excitation; the 30.5 kHz UFP component image clearly indicates the delaminations (in Fig. 39, right, dark colour).

6.2 NACE and defect-selective imaging

The scanning laser vibrometry suffers from variation of optical reflectivity; e.g. the measurements fail in the damaged areas with particularly strong scattering of laser light. Our experiments demonstrated that planar defects as localized sources of nonlinear vibrations efficiently radiate nonlinear airborne ultrasound. Such nonlinear air-coupled emission (NACE) is proposed as an alternative (and in many cases superior) methodology to locate and visualize the defects in NNDE [11].

6.2.1 Experimental observations of NACE

The feasibility of the NACE by nonlinear defects is illustrated in Fig. 40 which shows airborne acoustic fields at the fundamental frequency and its second harmonic radiated by a 40 kHz-flexural wave in a cracked rod (8x25x350 mm) of long-fibre CFRP. To visualize the airborne radiation field the technique of air-coupled vibrometry described in [12] was used. The fundamental frequency field in Fig. 40, left illustrates a classical propagation of a leaky flexural wave in the rod accompanied by a phase matched plane wave in air perturbed slightly by the presence of the defect.

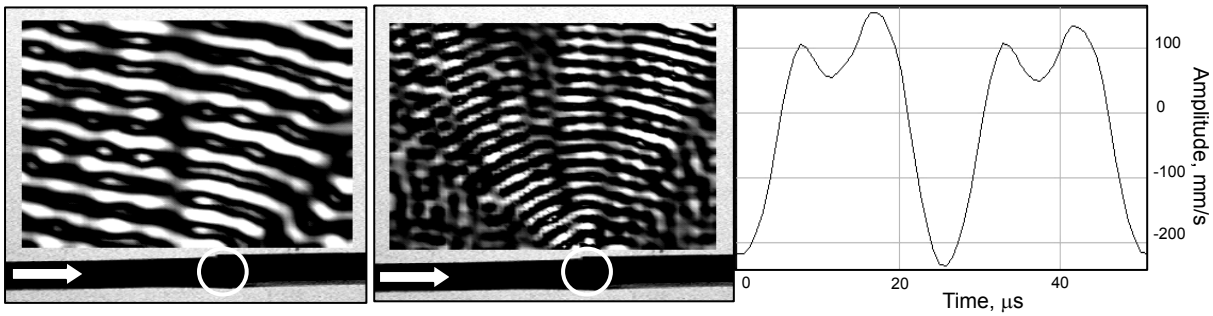

Fig. 40. Airborne fields above a cracked CFRP specimen: left - fundamental frequency (flexural wave propagates from left to right); middle - second harmonic pattern; waveform distortion in the crack area (right).

The second harmonic emission pattern (middle) reveals the two important features: firstly, it shows no radiation from outside the defect (circled in Fig. 40) and thus confirms the concept of a defect as a localized source of nonlinear emission. Secondly, the NACE directivity pattern consists of a few side-lobes and is therefore quite distinct from a cylindrical (or spherical) wave one would expect from a line (or point) source. The quantitative measurements showed that in this experiment the second harmonic is >15% of the fundamental wave signal. The high amplitude of the second harmonic is also confirmed by a strong nonlinear distortion of the local crack vibrations shown in Fig. 40, right.

The directivity of NACE radiation in the far field is an important factor to account for NDT-applications by nonlinear "listening" to defects. Mainly, the higher harmonic NACE fields observed feature a distinct directivity dominated by the two symmetrically slanted side-lobes. Such examples are shown in Fig. 41 for $25mm$-long delamination on the surface of a piezo-actuator embedded in a 1.5x35x350mm GFRP plate. The piezo-actuator itself was used for excitation of oppositely directed 50kHz elastic waves in the specimen.

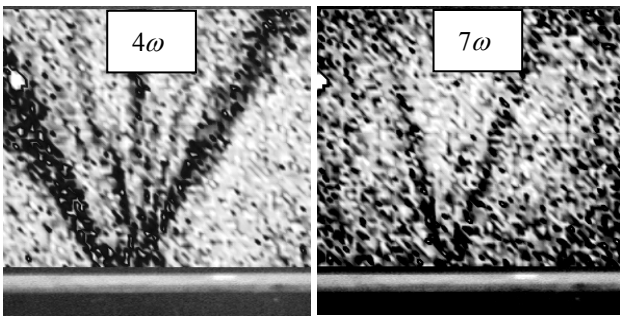

Fig. 41. NACE patterns for delamination in GFRP plate.

The directivity of the radiated field is known to be a spatial Fourier transform of the vibration velocity distribution in the source area [13]. The defect area is assumed to be a continuous distribution of the virtual nonlinear (n-th order higher harmonic) velocity sources over the length D:

$$w_n(x) = w_0 \Pi(x/D) \exp(jn\omega t), \quad (13)$$

where the rectangle function $\Pi(x/D) = 1$ for $|x| < D/2$ and zero otherwise.

The higher harmonic vibrations (13) are activated by the oppositely propagating waves in the specimen which introduce progressive time delay $\pm x/c$ in subsequent excitation of the higher harmonic sources so that $t \to t \pm x/c$ in (13). After this change the Fourier transform of (13) is found as follows:

$$W_n(\theta) = w_0 D\, sinc[(nKD/2)(\sin\theta \pm \sin\theta_0)], \tag{14}$$

where $\sin\theta_0 = c_{air}/c$.

According to (14), for $nKD > 1$, the directivity pattern displays two distinctive side-lobes steered to $\pm\theta_0$ from the specimen normal. The beam steering angle is determined by the well-known Cherenkov`s radiation condition. If $nKD < 1$, substantial radiation is expected at small angles θ. For small defects ($nKD << 1$), the radiation (14) becomes omnidirectional. These conclusions are supported by our experimental observations and the images in Figs. 40, 41, in particular. It is also worth noting, that the inverse Fourier transform of the directivity pattern (14) enables to evaluate the size of the defect (see 13).

For small angles of radiation and extended defect area, the symmetrical beams overlap and interfere to form the wave propagating along the normal to the specimen (the z-axis):

$$v(x,z) = 2v_0 \cos K_x x \cos(\omega t - K_z z)\ . \tag{15}$$

The NACE field observed for an extended delamination in a large fiber-reinforced concrete plate ($450x100x11mm$) is given in Fig. 42. The pattern is measured for a 40 kHz drive at 62 kHz NACE component originated from a frequency pair doublet of 18 kHz and 22 kHz. The standing wave distribution along the x-axis in (15) provides the system of vertical nodal lines in the airborne field. The anti-phase wave propagation along the z-axis in the adjacent channels stipulated by (15) is also clearly seen. The pattern in Fig. 42 indicates the formation of the standing wave in the delamination area and thus supports the approach based on the contra-flowing wave excitation of the defect area used above to interpret the NACE wave fields.

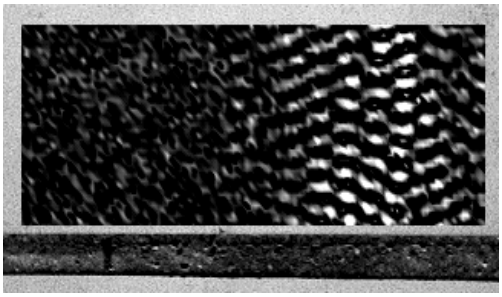

Fig. 42. NACE from an extended delamination area in a concrete plate.

6.2.2 Imaging of defects via NACE

A practical version of the NACE for nonlinear imaging of defects uses a high-frequency focused air-coupled ultrasonic transducer as a receiver to match the radiation directivity pattern (Fig. 43). The transducer high-frequency band-pass response combined with high-pass filtering circuit provides a strong rejection of the excitation frequency signal. The nonlinear frequency components are then used as an input to commercial air-coupled scanning equipment (AirTech 4000) for computer imaging of the NACE amplitude distribution over a specimen surface (C-scan).

In the experiments, the piezo-stack transducer and high-power supply (Branson Ultrasonics) provided an intense low-frequency excitation with $\geq 10^{-6}$ strain amplitude in the source. A pair of focused (focus spot ~2-3 mm, focus distance 40 mm) AC-transducers with frequency responses centred at ~400 kHz and ~450 kHz (3 dB-bandwidth of ~20 kHz) were alternately used as receivers in the C-scan mode. The two excitation frequencies around 40 and 20 kHz were used to maximize the NACE signals around (9-11th) and (23-24th) higher harmonics.

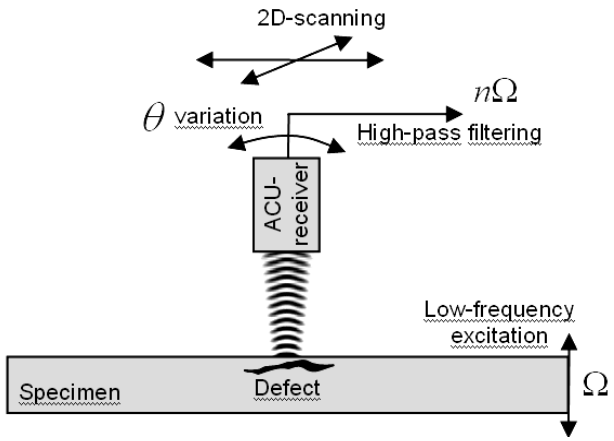

Fig. 43. Experimental set-up for NACE NNDE.

Unlike NSLV, which analyzes the light ***reflected*** from the specimen, the NACE-imaging relies on the direct nonlinear acoustic ***radiation*** by the defects. For the weakly-focused AC-transducers with cm-range depth of focus, the receiver is insensitive to medium scale variations of the surface profile. Our experiments show that the NACE operates well in various constructional materials (wood, concrete, metals) with raw surfaces and rugged defects in components, like bolted joints, arc welds, etc.

In Fig. 44, the NACE imaging results are compared with NSLV for multiple impact damage on a reverse side of a carbon fibre-reinforced multi-ply ($+45^0$; -45^0) composite plate (175x100x1 mm). Both techniques reliably visualize the defects with similar sensitivity.

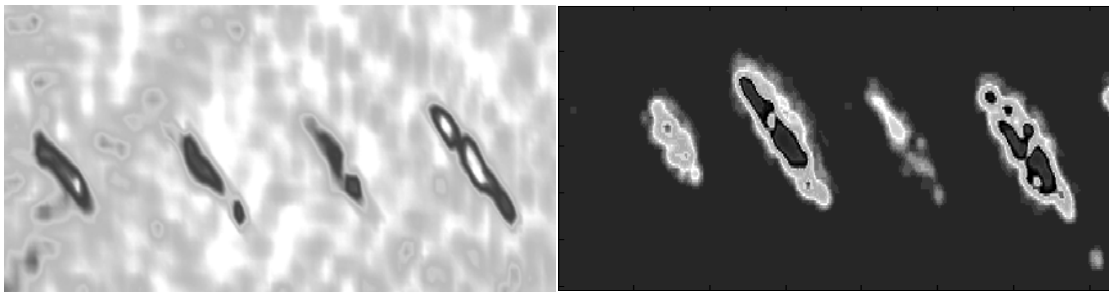

Fig. 44. Nonlinear imaging of an impact induced damage in multi-ply ($+45^0$; -45^0) CFRP-plate: laser vibrometry (second harmonic image, left); NACE (9^{th}-11^{th}) higher harmonic image (right).

The NACE high lateral resolution is illustrated in Fig. 45 which shows a photo (left) of (5x15 mm) delamination of specific shape in multi-ply GFRP plate. The mm-size contour details are reproduced closely in (9^{th}-11^{th}) NACE image (right).

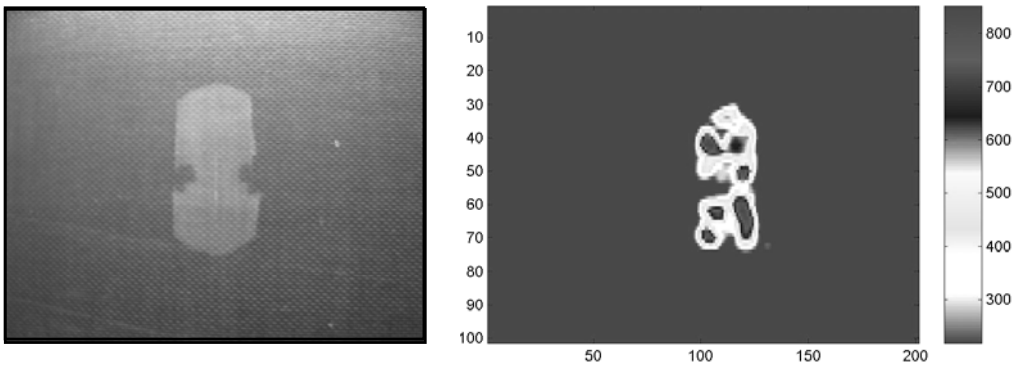

Fig. 45. NACE image (right) of 5x15 mm delamination (left) in GFRP multi-ply plate.

Fig. 46 (left) shows the (9-11^{th}) harmonic NACE image of the 50μm-wide fatigue crack in a steel plate (150x75x5 mm) with two horizontally located grip holes for cyclic loading at some distance from the crack. The image reveals that the NACE detects not only the crack itself but also the fatigue structural damage in the plasticity areas between the crack and the grip holes.
To verify the NACE sensitivity to micro-damage induced by plastic deformation, the NACE inspection was implemented for a steel specimen with a cold work area (5x40 mm) produced

by hammer peening. The image in Fig. 46, right confirms that the NACE develops even without serious cracked defects and clearly discerns the micro-damage induced by plastic deformation.

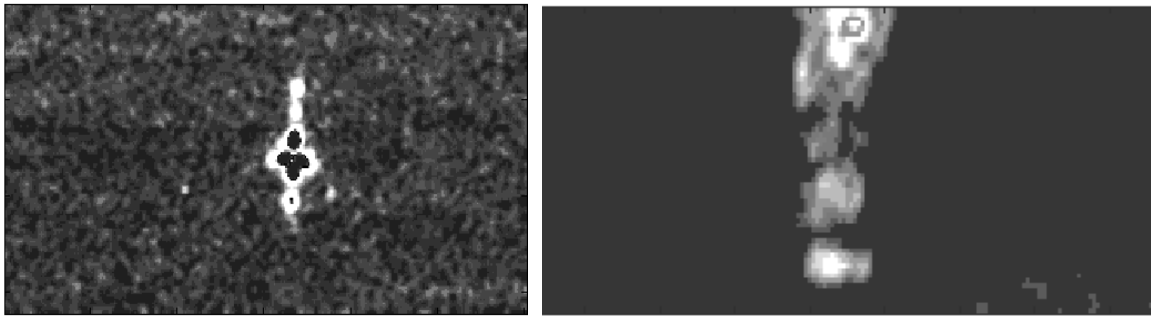

Fig. 46.NACE imaging in steel specimens (40 kHz-excitation): (9-11th) harmonic imaging of 50 μm-wide fatigue crack (left); (5x40 *mm*) hammer peening area in steel plate (right).

The NACE NDE-application was found to be particularly beneficial in metallic components where low acoustic damping facilitates the formation of standing waves which produce a strong spurious background in the NSLV. In particular, the images in Fig. 47 show that the NACE pattern reproduces well a quality of the laser weld-line between two steel components.

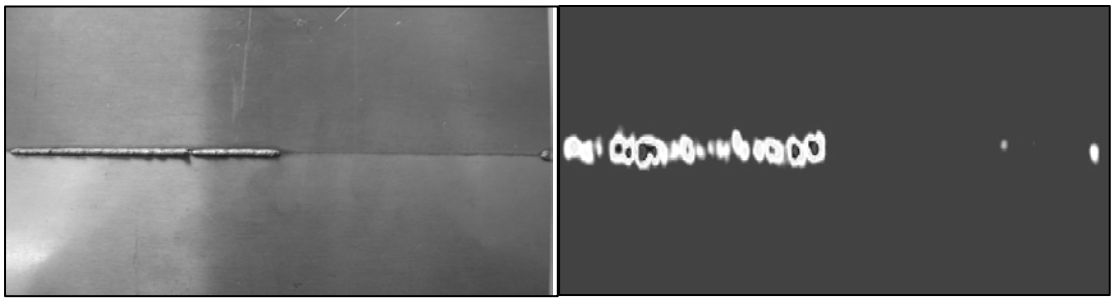

Fig. 47. Left – photo of the laser welded joint measured; right - NACE image of laser welded joint in steel.

7. Conclusions

The contact acoustic nonlinearity was shown to exhibit a substantial qualitative departure from fundamental nonlinear effects of higher harmonics generation in intact solid materials. The matter is that the stiffness of intact materials can be considered as a locally quasi-constant characteristic because even for high strains $\approx 10^{-4}$ the contribution of nonlinear terms in the stiffness variation is usually below 10^{-3}. As a result, noticeable nonlinear effects are developed only because of accumulation of the nonlinear response along the propagation distance.

On the contrary, the ultrasonic wave interaction with a cracked defect is accompanied by a strong step-wise local stiffness variation: the stiffness of the crack can be substantially greater for compression than for tensile stress if the wave amplitude is high enough to cause an intermittent contact between the crack surfaces. In this case, the intact material outside the defect can be considered as a “linear carrier” of the elastic wave while the defect is a localized source of nonlinearity.

At moderate driving amplitude, the CAN suggests a fully deterministic scenario with higher harmonic generation and/or wave modulation. These effects feature anomalously high

efficiency, specific dynamic characteristics, and unconventional "rectified" waveform distortion. For the higher excitation amplitude, the mechanical instability phenomena well known in other branches of nonlinear physics can develop in the defect area. The lower stiffness of the cracked area makes it behave as a localized oscillator which is, apparently, strongly nonlinear due to CAN. Therefore, for an intense acoustic excitation it can manifest such effects as subharmonic generation, instability and transition to chaotic dynamics. As a result, the spectrum of local oscillations acquires a number of new frequencies (ultra-subharmonics and ultra-frequency pairs). All the nonlinear spectral components demonstrate a strong localization in the defect areas.

This feature of localized nonlinearity enables 2D-imaging of the nonlinear excitations confined inside the defect areas. Thus, nonlinear NDT of imperfect materials via CAN is inherently defect-selective, i.e. it distinctively responds to fractured flaws. Fortunately, this group of flaws includes the most malignant defects for material strength: micro- and macro-cracks, delaminations, debondings, impact and fatigue damages.

A number of case studies prove their applicability for nonlinear NDE and defect-selective imaging in various materials by using NSLV and NACE. Particularly successful examples include hi-tech and constructional materials: impact damage and delaminations in fibre-reinforced plastics, fatigue micro-cracking and cold work in metals, delaminations in laminates and fibre-reinforced concrete.

Unlike conventional ultrasonic testing, the NNDT provides abundant multi-frequency information on properties and location of defects. This suggests an opportunity for application advanced data and image fusion algorithms to result in higher sensitivity and accuracy of inspection, greater reliability and quality of NDT.

Acknowledgement

The authors are grateful to the German Research Foundation for supporting this work as part of the project Bu 624/33-1 ("Akustische Nichtlinearität als selektiver Defektindikator in der zerstörungsfreien Prüfung").

References

1. I.Yu. Solodov, Ultrasonics, v. 36, 383 (1998)
2. I.Yu. Solodov, N. Krohn, and G. Busse, Ultrasonics, v. 40, 621-625 (2002)
3. C. Pecorary and I. Solodov, Non-classical nonlinear dynamics of solid interfaces in partial contact for NDE applications. In: *Universality of Non-Classical Nonlinearity with Application to NDE and Ultrasonics,* Ed. P. Delsanto, Ch. 19, 307-324, Springer Verlag, New York, USA (2006)
4. K. Pfleiderer, Ph.D. Thesis, Stuttgart University (2006)
5. I. Solodov, J. Wackerl, K. Pfleiderer, G. Busse, Appl. Phys. Lett., v. 84, 5386-5388 (2004)
6. I. Solodov, K. Pfleiderer, and G. Busse, Nonlinear acoustic NDE: inherent potential of complete non-classical spectra. In: *Universality of Non-Classical Nonlinearity with Application to NDE and Ultrasonics,* Ed. P. Delsanto, Ch. 29, 465-484, Springer Verlag, New York, USA (2006)
7. N. Minorsky, *Nonlinear Oscillations*. D. Van Nostrand Co. Inc., Princeton (1962)
8. N. Krohn, K. Pfleiderer, I. Solodov, and G. Busse, Rev. Progress in QNDE, Eds. D.O. Thompson and D. Chimenti, v. 22**,** 981-988 (2002)
9. I. Solodov and B. Korshak, Phys. Rev. Lett., v. 88, 014303 (2002)
10. E.M. Ballad, B.A. Korshak, I.Yu. Solodov, N. Krohn, and G. Busse, Nonlinear Acoustics at the Beginning of the 21st Century, Eds. O. Rudenko and O. Sapozhnikov, pp. 727-734 (2002)
11. I. Solodov and G. Busse, Appl. Phys. Lett., v. 91, 251910 (2007).
12. I. Solodov, D. Döring, and G. Busse, Appl. Optics, v. 48, 7, (2009)
13. E.G. Williams, Fourier Acoustics: Sound radiation and nearfield acoustical holography, Academic Press, New York (1999).